Geochemistry, Geophysics, Geosystems®

AGU ADVANCING EARTH AND SPACE SCIENCES

RESEARCH ARTICLE
10.1029/2024GC011573

Monitoring Salt Domes Used for Energy Storage With Microseismicity: Insights for a Carbon-Neutral Future

Joses Omojola[1] and **Patricia Persaud**[1]

[1]Department of Geosciences, University of Arizona, Tucson, AZ, USA

Key Points:

- Passive seismic monitoring with surface arrays is a non-invasive approach for identifying hazards in salt domes
- Microearthquakes detected with our finetuned machine learning model illuminate shear zone geometries and structural hazards
- Cavern storage wells drilled within proximity of shear zones are at risk of safety incidents

Supporting Information:

Supporting Information may be found in the online version of this article.

Correspondence to:

J. Omojola,
jomojo1@arizona.edu

Citation:

Omojola, J., & Persaud, P. (2024). Monitoring salt domes used for energy storage with microseismicity: Insights for a carbon-neutral future. *Geochemistry, Geophysics, Geosystems*, *25*, e2024GC011573. https://doi.org/10.1029/2024GC011573

Received 22 MAR 2024
Accepted 27 OCT 2024

Author Contributions:

Conceptualization: Patricia Persaud
Data curation: Joses Omojola, Patricia Persaud
Formal analysis: Joses Omojola, Patricia Persaud
Funding acquisition: Patricia Persaud
Investigation: Joses Omojola, Patricia Persaud
Methodology: Joses Omojola, Patricia Persaud
Project administration: Patricia Persaud
Resources: Patricia Persaud
Supervision: Patricia Persaud

Abstract Underground storage in geologic formations will play a key role in the energy transition by providing low-cost storage of renewable fuels such as hydrogen. The sealing qualities of caverns leached in salt and availability of domal salt bodies make them ideal for energy storage. However, unstable boundary shear zones of anomalous friable salt can enhance internal shearing and pose a structural hazard to storage operations. Considering the indistinct nature of internal salt heterogeneities when imaged with conventional techniques such as reflection seismic surveys, we develop a method to map shear zones using seismicity patterns in the US Gulf Coast, the region with the world's largest underground crude oil emergency supply. We developed and finetuned a machine learning algorithm using tectonic and local microearthquakes. The finetuned model was applied to detect microearthquakes in a 12-month long nodal seismic dataset from the Sorrento salt dome. Clustered microearthquake locations reveal the three-dimensional geometry of two anomalous salt shear zones and their orientations were determined using probabilistic hypocenter imaging. The seismicity pattern, combined with borehole pressure measurements, and cavern sonar surveys, shows the spatiotemporal evolution of cavern shapes within the salt dome. We describe how shear zone seismicity contributed to a cavern well failure and gas release incident that occurred during monitoring. Our findings show that caverns placed close to shear zones are more susceptible to structural damage. We propose a non-invasive technique for mapping hazards related to internal salt dome deformation that can be employed in high-noise industrial settings to characterize storage facilities.

Plain Language Summary In the shift toward renewable energy, underground storage is vital for increasing the feasibility of fuels like hydrogen. Salt formations are ideal for storage, and caverns in salt domes are used worldwide to store vast amounts of energy reserves. But salt domes can become unstable and lead to cavern collapse, posing risks to the environment and nearby communities. Traditional methods are expensive, often require drilled wells, and do not always spot hazards. We instead used recordings of ground shaking from small earthquakes to identify them. By collecting these recordings for over a year with an array of instruments installed at the surface over a Louisiana salt dome, we were able to develop a new method for identifying very small earthquakes, allowing us to pinpoint hazardous areas. Our approach offers a non-invasive way for scientists and engineers to assess hazards and mitigate risks associated with drilling and underground storage operations in salt domes.

1. Introduction

The expansion of underground facilities capable of safely storing vast amounts of renewable energy resources is a key component of the energy transition. Storage plays an important role in balancing supply and demand by stockpiling excess energy and providing a reliable backup during peak demand periods (Juez-Larré et al., 2019). Seasonal energy demands have driven the need for underground storage facilities since 1915, for example, over 20% of the natural gas consumed in the United States each winter comes from underground storage facilities (Beckman et al., 1995). Globally, over 148 sedimentary basins have salt formations suitable for underground storage of fuels such as hydrogen, natural gas, and unrefined petroleum products, but most of the storage activity has been limited to technologically advanced countries in Europe, Asia, and North America (Gillhaus & Horvath, 2008). In the United States, underground storage is utilized in three major types of subsurface environments: depleted oil and gas fields, aquifers, and salt caverns. The Gulf Coast states of Louisiana (Figure 1a) and Texas have numerous salt domes (>90% of cavern fields in the US) and the largest facilities for state-level gas storage in the country (Lord, 2009). They have the world's largest supply of emergency crude oil, which is stored underground at four sites of the United States Strategic Petroleum Reserves (SPR, 2022), and are well positioned to expand salt cavern capacity to meet increasing energy demand.

Visualization: Joses Omojola
Writing – original draft: Joses Omojola
Writing – review & editing: Joses Omojola, Patricia Persaud

Salt domes are extensively used for underground storage because of their favorable geomechanical properties, large storage capacity, and low cushion gas requirements (Caglayan et al., 2020). They are relatively safe; however, the presence of internal shear zones within these salt structures can potentially compromise their stability and long-term functionality (Bérest et al., 2019; Looff, 2017). A study of safety incidents at underground storage facilities across the United States determined that subsurface and well integrity problems contributed to 89% of recorded incidents in salt caverns, compared to 44% in depleted oil and gas fields and 68% in ground water aquifers (Evans & Schultz, 2017). Subsurface incidents in salt domes have been linked to caprock instability, overburden faulting, and boundary shear zones (Evans, 2007; Looff, 2017; Warren, 2017). Boundary shear zones in salt domes are generally zones of impurities where surface water and hydrocarbons have led to the formation of vugs, voids, or recrystallization of salt, making it weak and friable under moderate conditions, or volatile and explosive under extreme conditons, where the rock salt has been infused with gas (popping salt) (Davison, 2009; Jacoby, 1977; Warren, 2017). Laboratory studies of normal Gulf Coast salt reveal that it is dominated by uniform grain sizes (~3–10 mm diameter) of halite with banded layers or structureless features (Kupfer, 1990). Deviations from this norm, such as high concentrations of anhydrite, potash salts, and impurities, can create anomalous salt features (Davison, 2009; Looff, 2017). Multiple anomalous features aligned within a zone can form boundary shear zones (BSZs). Field studies of boundary shear zones exposed within salt mines reveal that they can range in size from several meters to kilometers and may traverse entire salt domes (Davison, 2009; Jackson et al., 2015; Jacoby, 1977) (Figure 1d). Unlike faults, BSZs can form through independent processes such as hydrocarbon generation within embedded shales that are not necessarily related to tectonic events (Warren, 2017). They often occur at salt spine boundaries (see Figure 1c) due to differential upward movement of the spines. Using current techniques, little to no information on shear zone emplacement is known at the onset of underground storage projects, and wells are drilled using geomechanical models that are focused on optimizing cavern design while overlooking shear zone hazards (Wijermars, 2013).

The study of boundary shear zones (BSZ) in salt domes is crucial for various reasons. Firstly, accurate mapping and characterization of BSZs help improve development strategies for early-stage underground storage projects by helping operators optimize cavern placement. Secondly, understanding the seismic behavior of shear zones is essential for assessing the risk of failure or leakage of wellbores in developed facilities, and early detection of casing or cavern collapse, because placement near or within BSZs increases the potential for accidents due to reduced salt-structure quality (Jacoby, 1977). Accidents in salt domes highlight the critical importance of studying subsurface hazards for both residents and the environment alike. Between 1959 and 2012, over 26 incidents occurred at salt domes in the US (Ford & Dreger, 2020; Warren, 2017). Casing failures at salt domes have caused fires, resident evacuations, and extensive damage to infrastructure and the environment amounting to millions of dollars (Evans, 2007). A cavern collapse along a disturbed rock zone at the Napoleonville salt dome in Bayou Corne, Louisiana, in 2012 destroyed cypress trees within a 12-acre sinkhole, forced evacuations of nearby residents due to gas leaks from collapsed caverns, and cost the operating company over $225 million in buyouts, remediation, and monitoring costs (Hanusik & Katy, 2019; Mitchell, 2018). In 1992, subsurface instability at the Weeks Island salt mine in Louisiana resulted in the formation of a 10-m wide sinkhole, requiring $100 million for draining and remediation of existing caverns (Bauer et al., 1997; Neal & Myers, 1994; Warren, 2017). They are also prone to outbursts, which can be as large as the Belle Isle and Morton mine incidents that released over 600,000 and 50 million standard cubic feet (scf) of gas and led to the loss of miners' lives at Belle Isle (B. Ehgartner et al., 1998; Plimpton et al., 1980; Warren, 2017).

To mitigate incidents in salt domes, shear zone mapping can be conducted using various techniques. Sonar measurements and well logs have been utilized to identify boundary shear zones (BSZs) in salt domes (Looff, 2017). 3D and 2D seismic surveys have been used to characterize caprock geometric anomalies at domes and assess their potential seismic hazards (Neal et al., 1993; Rautman et al., 2010). Foliation of halite crystals from cores has helped map boundary shear zones that were not detected by reflection seismic surveys (Seni et al., 1984). However, some of the shortcomings associated with mapping shear zones using the techniques above are limited spatial samples from well data, and insufficient 3D seismic resolution within salt deposits, which limits mapping of the shear zone outline to only along the overlying caprock (Looff, 2017; Neal et al., 1993; Rautman et al., 2010). One way of constraining the location of boundary shear zones is microearthquake monitoring. Passive seismic monitoring has been used to detect seismic events such as rock falls, sliding motion, and fault movement within salt domes (Ford & Dreger, 2020; Fortier et al., 2006). Although more affordable than borehole installations, one challenge with surface seismic monitoring is that the recordings of small magnitude

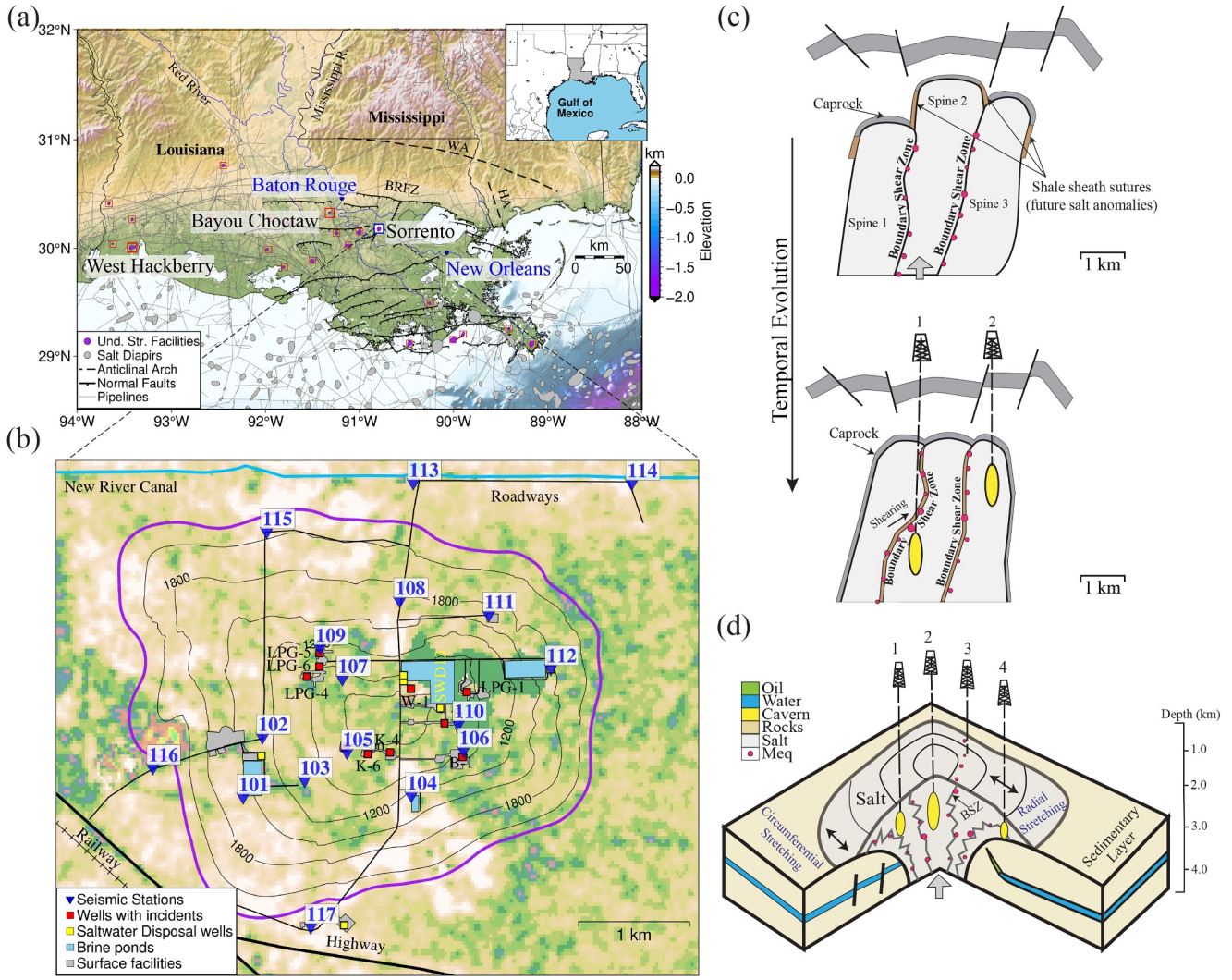

Figure 1. Overview of the Sorrento salt dome location and the evolution of boundary shear zones. (a) Regional map of salt domes in the US Gulf Coast, Louisiana and northern Gulf of Mexico. Domes used for underground storage are highlighted with red squares. The two US Strategic Petroleum Reserves and Sorrento domes are annotated. The map also shows regional structural features from Gillhaus and Horvath (2008) and gas pipelines with gray lines (EIA, 2012). Regional structural features are BRFZ—Baton Rouge Fault Zone; HA—Hancock Arch; WA—Wiggins Arch. (b) Expanded map of the Sorrento salt dome showing the locations of the stations in the seismic array (for March–April 2022), and wells discussed in the text. Black contour lines indicate the top of the salt (Looff, 2017), and the outline of the dome is in purple. (c) Sketch depicting the development of shear zones in salt domes through time (Warren, 2017). Microearthquakes (meq) are shown with magenta circles. (d) 2.5D schematic representation of the shear zone extent in a salt dome with overlying graben mimicking the Sorrento dome's geology.

events can be masked by local equipment noise and anthropogenic sources. This can severely inhibit event detection and location methods that use travel-time techniques (Kinscher et al., 2015; Mercerat et al., 2009). Post-accident investigations of some safety incidents at salt domes have detected seismicity prior to cavern collapse (Dreger & Ford, 2020; Mercerat et al., 2009); however, the connection between shear zones and seismicity remains unclear.

Cavern operator reports of ground shaking at the Sorrento salt dome in Ascension Parish, Louisiana, in January 2020 motivated us to install the SORRENTO array and investigate the subsurface hazards and physical processes affecting drilled wells and excavated caverns. The Sorrento salt dome is a slightly elongated salt diapir with an overlying graben system. The salt body has a spatial extent of approximately 5 km 4 km (Looff, 2017) (Figure 1b). It is located in the Pontchartrain basin, where over one third of Louisiana's population lives. Surface conditions are swampy with an average elevation of 5 m above sea level. The area gets flooded regularly following heavy rainfall and storms, sometimes restricting physical access to deploy and retrieve seismometers. The dome is

40 km SE of the state capital, 70 km NW of New Orleans, Louisiana and <19 km from the Maurepas swamp and wildlife management area (Figure 1a). Salt layers are relatively shallow (1,524 m depth), and oil and gas production occurs in flank traps to the north and south. The field has produced over 750 billion cubic feet (bcf) of gas and 5,000 million barrels of oil (mbo) (Petroleum, 2009), and saltwater is being disposed in layers between 310 and 495 m depth on the eastern and western flanks of the dome (Consultants, 1990).

Currently, underground storage caverns within the Sorrento salt dome have a storage capacity of 8.92 (bcf) of gas (SONRIS, 2024). Prior incidents resulted in the abandonment of two early cavern wells (Looff, 2017) when anomalous salt features were encountered during drilling and leaching. In May 2021, during monitoring, ground movement along a shear zone damaged the LPG-5 cavern (Figure 1b), releasing 220,000 scf of nitrogen during a mechanical integrity test, and creating a 6–9 m wide by 1.5 m deep crater on the ground surface beneath the wellhead (LADNR, 2020a, 2021a).

In this study, we focus on monitoring seismic activity to identify zones of inferior salt quality that can impact the integrity of well and cavern operations. We demonstrate with a 12-month-long seismic dataset that seismicity can be linked to boundary shear zones at the Sorrento dome, and analyze its connection to a recent storage cavern failure. We located clusters of seismicity that can be used to identify unstable zones within salt, and extended mapping of known shear zones away from well control. We believe this study can serve as an analog for how storage caverns at other salt domes may be monitored to prevent future accidents, and highlight the importance of understanding subsurface hazards as more cavern facilities are being developed to meet rising energy storage needs.

2. Data

Our analysis was conducted using a combination of waveforms from nodal seismometers, sonar surveys, and well data. The SORRENTO array comprised 17 stations installed across the dome (Figure 1b) to record seismic data for 12 months. Each station was occupied with a three-component SmartSolo 5 Hz nodal seismometer with a self-contained GPS antenna and battery that recorded at 500 Hz. Nodal seismometers were selected because of their ability to be submerged underwater and deployed without the need for solar panels. We buried the nodes in ∼20-cm deep holes, covered with a couple centimeters of soil to reduce the impact of noise from the nearby highways, oilfield equipment, and frequent storms. The nodes were deployed in a loosely circular grid depending on site accessibility to provide coverage around the flanks and major cavern clusters near the center of the dome. Interstation distances varied between 0.2 and 1.9 km, and most sites were re-occupied during the 12 1-month installations that occurred between February 2020 and July 2022 (Table S1 in Supporting Information S1). Raw waveforms in counts were downloaded from the nodes and the corresponding instrument response file was obtained from the IRIS Nominal Response Library. We detrended the waveforms and converted them to displacement using standard procedures from the ObsPy package (Krischer et al., 2017).

Sonar surveys are acquired by cavern operators every 5 years in line with compliance requirements dictated by the Louisiana Department of Natural Resources (LADNR), and we digitized sonar surveys for caverns with available reports. Additionally, we analyzed the survey reports and well data available at the LADNR SONRIS website (SONRIS, 2024). Event information for regional and teleseismic earthquakes with magnitudes $>M_w$ 5 were obtained from IRIS and the USGS to evaluate the possibility of external triggering of salt dome microearthquakes.

3. Methodology

3.1. Event Detection and Phase Picking

We initially employed the traditional short-term-average/long-term-average (STA/LTA) methods for event detection with limited success. The STA/LTA technique resulted in a large number of false positive detections originating from the operating equipment around the dome. We proceeded to test popular machine learning phase-pickers such as EQTransformer and PhaseNet (Mousavi et al., 2020; Zhu & Beroza, 2019) for microearthquake detection. Adjusting the parameters of the machine learning models reduced some of the false positive detections but limited detection of many of the small microearthquakes (Text S2 and Figure S1 in Supporting Information S1). To achieve a balance between microearthquake detection and minimizing false positives, we developed and trained a hybrid U-Net model described below (Figure 2a) for event detection and phase picking on salt dome microearthquakes. We trained the base hybrid U-Net model using a subset of the Stanford Earthquake Dataset

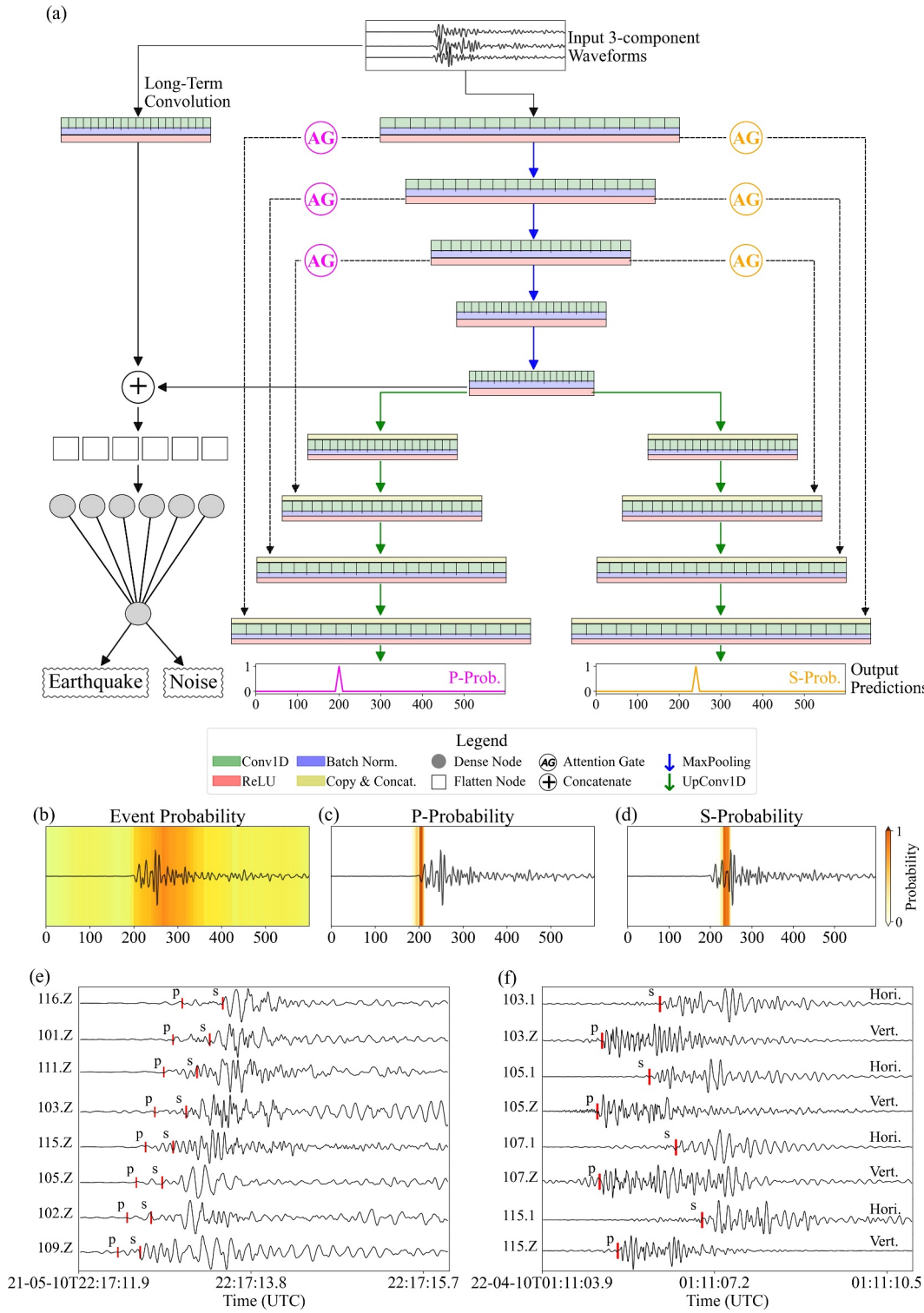

Figure 2. The hybrid U-Net model for seismic event detection. (a) Architecture of the detection model showing input waveforms and output predictions. Each convolution layer has three kernels with n-filters. Input dimensions reduce by two for each encoding layer, and increase by two for each decoder layer. (b–d) Gradient class activation map (Grad-CAM) of the model's event, P-wave, and S-wave detection probability. Hot colors have higher probabilities. (e) Vertical displacement waveforms from the microearthquake (event 19) recorded during the mechanical integrity test (MIT) at the LPG-5 cavern, showing impulsive P-wave arrivals. (f) Examples of vertical and horizontal waveforms from a microearthquake detected with the hybrid model showing P- and S-wave arrivals, respectively.

(STEAD) (Mousavi et al., 2019), and finetuned the model weights using manually selected salt dome micro-earthquakes from the initial recordings at Sorrento. The finetuned model predicts event detection probabilities and the position of body wave arrivals simultaneously.

The finetuned model was applied to 6 s long sliding windows with a step size of 4 s extracted from the Sorrento array. An event was recorded when a minimum of four adjacent stations were triggered (detection probability from the hybrid U-Net >95%, and phase probabilities >50%) within a 6 s time window. This served as a simple association method, and thresholding the detections across both the array and at each individual station helped with eliminating false positive detections or spikes that could be localized at individual stations. Associated picks were manually quality checked to remove outlier detections, and improve the quality of the event location process.

3.1.1. Waveform Preprocessing

Training data for the base model were obtained from a subset of the Stanford Earthquake Dataset (STEAD) (Mousavi et al., 2019). We filtered the STEAD catalog to select only events with magnitudes $M_w < 3$ and epicentral distances <5.5 km to mimic the expected seismic activity at Sorrento (Figure S2a in Supporting Information S1). The subset included (200 K) event and noise waveforms randomly split into training, validation, and test sets (90%, 5%, 5%). Five hundred salt dome event and noise waveforms were manually selected to finetune the model and the data was downsampled to 100 Hz. The finetuning waveform data were split in a similar manner to the base model waveforms. Binary labels were used for event detection, and phase pick labels were generated by convolving a triangular function with the onset time of the phase picks (Figure 2a).

3.1.2. Model Training and Evaluation

We modified the Attention U-Net (Oktay et al., 2018; Ronneberger et al., 2015) for 1D convolution (Figure 2a). The input for the model consisted of 3-component waveforms cropped into 6-s long recordings and downsampled to 100 Hz. The training data were augmented by randomly shifting the event origin within the 6-s window. A single convolution layer with longer kernels was appended to the vanilla Attention U-Net to mimic the LTA and we refer to this layer as a long-term-average convolution (LTC) layer (Figure 2a). Using the LTC layer further stabilized the event detection weights during training and improved the validation loss (Figure S2b in Supporting Information S1). The input waveforms were passed through four down-sampling convolution layers, and rectified linear unit (ReLU) activation, batch normalization and same padding were applied to each layer (Glorot et al., 2011; Ioffe, 2015). We split the bottle-neck convolution output into three, where one of the outputs was concatenated with the LTC output and passed through a series of dense layers to produce a binary classification of either event or noise. The remaining two outputs from the bottle-neck layer were concatenated with skip connections from attention gates and upsampled to match the number of triangular label samples used for P- and S-arrivals (Figure 2a). We used the sigmoid activation function to set probabilities for the final layers of all the model outputs

$$S(x) = \frac{1}{1+e^{-x}} = \frac{e^{x}}{e^{x}+1} = 1 - S(-x) \tag{1}$$

We used the binary cross-entropy loss function, which computes the following average:

$$\text{Loss} = -\frac{1}{\text{output size}} \sum_{i=1}^{\text{output size}} y_i \,.\, log\ \hat{y}_i + \left(1 - y_i\right) . \log\left(1 - \hat{y}_i\right) \tag{2}$$

where $\hat{y}_i$ is the i-th scalar in the model output, y_i is the corresponding target value, and the output size is the number of scalar values in the model output. The output from the phase picker model head is a probability distribution for all points in the input timeseries. We stopped training after the validation loss did not improve for 10 consecutive epochs. The diagnostic accuracy of the model measured with the Area under the Curve (AUC) for the Receiver Operating Characteristic (ROC) was 1 on the STEAD data, and 0.996 on the Sorrento events. AUC values denote the confidence of correct predictions from classification models, values of 0.5 indicate random predictions, and values of 1 indicate that the model will correctly predict a random positive event. Additional

evaluation metrics used to assess model performance are described in Text S2 in Supporting Information S1. Grad-CAM maps show segments of a waveform that the finetuned model pays attention to for classifying events and picking phase arrivals (Figures 2b–2d).

3.2. Event Location and Magnitude Estimation

Prelimary event locations were estimated using the HYPOINVERSE 1.40 program (Klein, 2002). No local velocity model exists for this area, and a 1D velocity model was obtained from the sonic logs of the Exxon SWD-13 well (Schlumberger, 2004). A constant replacement velocity of 4.0 km/s was used for deeper salt layers and a V_p/V_s ratio of 1.72 was selected based on previous salt dome studies (Kinscher et al., 2015; Nayak & Douglas, 2014). Event trial depths were fixed at 500 m near the salt-sediment boundary, and a relocated catalog was estimated using the double-difference method of the HYPODD program (Waldhauser, 2001). Monte Carlo simulations of best fit fault planes through the clustered relocated catalog were calculated using a hypocenter-based 3D imaging method (Truttmann et al., 2023). Additional details are provided in Text S3 and Figure S3 in Supporting Information S1.

We calculated the local earthquake magnitude (M_L) by removing the instrument response to obtain displacement waveforms. The seismograms were bandpass filtered between 0.1 and 50 Hz and windowed 0.5 s before and 2 s after the P-arrival. The peak amplitude A_{max} is computed within this window and the local magnitude is expressed as follows:

$$M_L = \log_{10}(2800.\, A_{max}) + 1.27.\, \log_{10} D + a \tag{3}$$

Where A_{max} is the maximum displacement in mm, D is the hypocentral distance in km and $a = 0.377$ for events located <40 km from the station (Di Grazia et al., 2001). The local magnitude for each station was estimated, and the median of all stations was selected as the final magnitude for each event. Since a magnitude scale has not been developed for the Louisiana Gulf Coast, the absolute values of the magnitudes may vary; however, they provide a good indication of the relative size of events.

3.3. Focal Mechanisms

Because we had a limited 1D velocity model, we inverted P-polarities to compute focal mechanisms for the relocated events. Waveform inversion methods such as the MTtime algorithm would also require filtering waveforms at frequencies below 0.1 Hz, which is outside the frequency band for resolving microearthquakes. Spectral gates were used to denoise the raw waveforms and improve the identification of P-wave polarities (Figure S4 in Supporting Information S1) (Sainburg et al., 2020), and the P-wave polarities of the first arrivals were manually picked. A minimum of eight stations were required for calculating focal mechanisms. Considering the polarity uncertainty of emergent waveforms, we allow provisions for pick uncertainty up to 20% within the polarity inversion workflow. Preferred fault plane orientations were calculated by performing a grid search every 5° for 50 trial runs with the HASH program (Hardebeck & Shearer, 2008). Additional perturbations of the input velocity model, take-off angles, and event locations constrained within the relocation error limits were used to quantify the uncertainty for each fault plane solution.

4. Results

We use waveform duration, event onset, and apparent velocities to classify the events detected by our hybrid U-Net model into two main types of microseismic (MS) events and designated them MS-I and MS-II. The MS-I events have high-frequencies (5–40 Hz), and fast P-wave travel-times of <1 s across the array (Figures 2e and 2f) and their temporal distribution is shown in Figure 3a. The 152 MS-I events exhibit a combination of emergent and impulsive waveform onsets with attenuated amplitudes over short distances suggestive of local scattering and potential absorption from gas-filled caverns. Local magnitudes for these events range between M_L −3 and 2, with an average magnitude of −1.54, and a median of −1.68. The MS-I events were relocated using the HYPODD program (Waldhauser, 2001). In contrast, the 1019 MS-II events (Figure 3b) have impulsive waveforms (Figure S5 in Supporting Information S1) with slower apparent travel-times of <500 m/s. These events have higher frequencies (70–100 Hz) compared to MS-I events and their delayed wavespeeds have limited our ability to locate

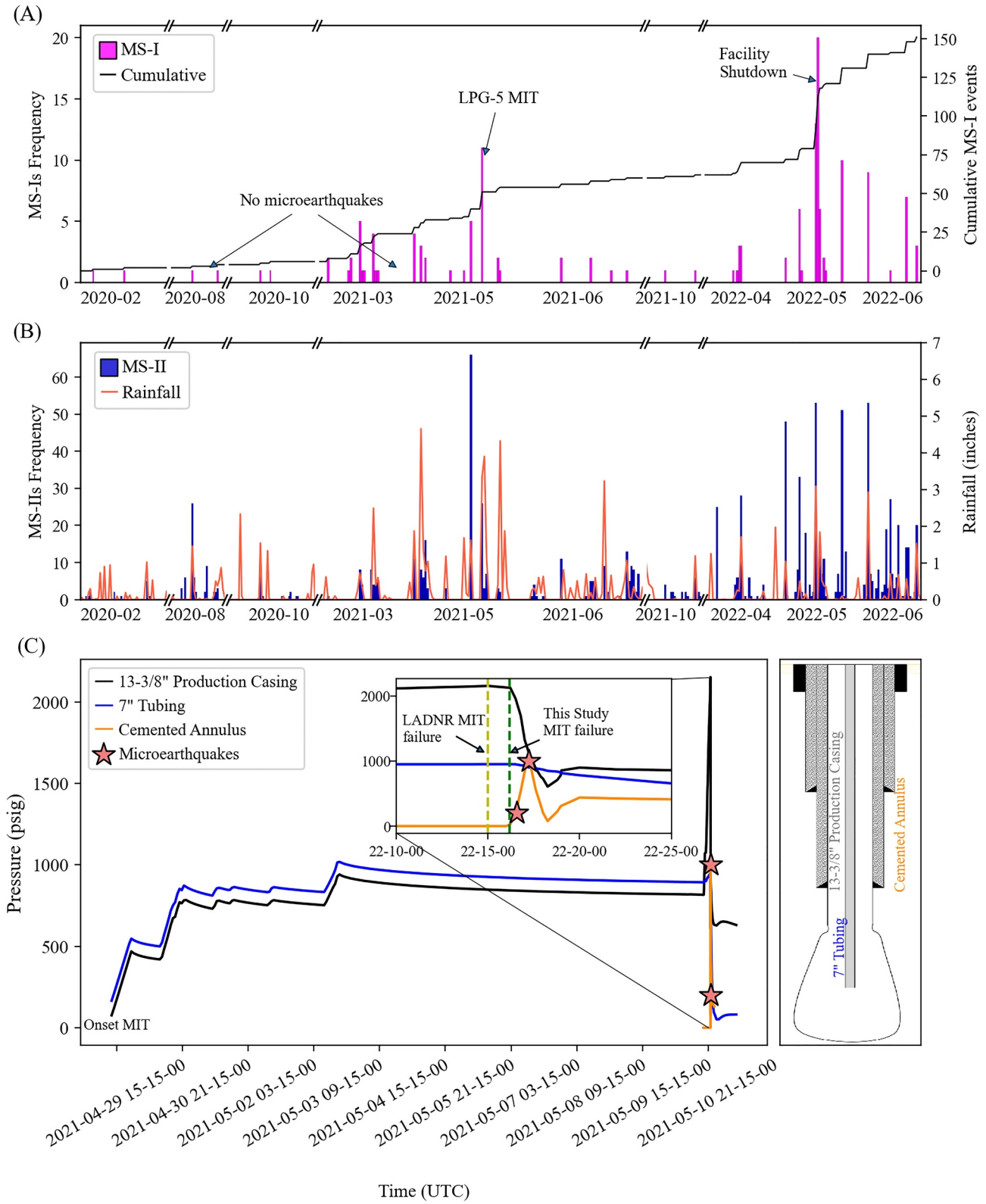

Figure 3. Temporal distribution of microearthquakes and cavern pressure. Data acquisition gaps are indicated as breaks along the *x*-axis. (a) Histogram of daily number of MS-I (microearthquakes) recorded at Sorrento (magenta) showing the mechanical integrity test (MIT) failure and facility shutdown. (b) Histogram of daily number of MS-II events (blue) with rainfall overlay (red lines). (c) Pressure profile of the LPG-5 cavern during the MIT showing coincidence between the microearthquake timing and annulus pressure spike. The well schematic on the right highlights the position of different casing types downhole.

them. Their waveform amplitudes were large enough to be recorded across the dome, indicating a significant energy source.

4.1. Temporal Seismicity Trend

The MS-I events exhibit random cascade-like peaks followed by periods of quiescence (Figure 3a). The rate of activity for MS-I was less than five events per day for most of the study period; however, the seismicity rate doubled on 10 May 2021, when the LPG-5 well failed a mechanical integrity test. We also observed a second spike in the number of microearthquakes when background noise levels decreased due to a facility shutdown and workover activity at the W-4 well (LADNR, 2022b). No aftershock sequence suggestive of intermittent deformation pulses that weaken over time was observed in the catalog (Nayak & Dreger, 2018). Swarms of MS-II events were observed to coincide with heavy rainfall periods (Figure 3b), and further investigation into potential sources is planned for a subsequent study.

4.2. Local Seismicity Along Shear Zones

Prior to making any geological interpretations, we evaluated the reliability of the event locations. An event location is considered reliable if it was recorded by a minimum of four stations with computed location errors <50 m and travel time residuals <30 ms. We obtained high-quality hypocenter locations for 129 of the 152 detected MS-I microearthquakes. A large number of events originate within the dome at depths between 0.2 and 4 km, spread out along two zones in the N-S direction, and are separated by a noticeable gap in seismicity around the W-1 cavern (Figure 4a). Some normal faults above the salt also strike roughly N, but the clustered events are not aligned along any of these faults. Large magnitude events were detected close to caverns with well incidents (Figure 4a) and few events were observed outside the salt boundaries.

The two zones of clustered seismicity (dashed lines in Figures 4a and 4c; Figure S6 in Supporting Information S1) have dimensions of ∼2 km along strike, that extend to ∼1–3 km depth with varying widths. Reports from the LPG-2 well located ∼76 m north of LPG-1 (Looff, 2017), that was drilled between two salt spines and intersected the eastern cluster of seismicity, confirm the presence of two salt walls that are indicative of boundary shear zones (BSZ) (Figure 5b). We therefore interpret that the two clusters of seismicity are associated with salt movement along boundary shear zones that we abbreviate as the west and east BSZs. Both shear zones have near-vertical dips that are confirmed by the focal mechanism solutions (>80°E).

Seismicity along the west BSZ is diffuse and twice as dense as seismicity along the east BSZ. In the east BSZ, the miroearthquakes are clustered within a 200 m wide zone (Figure 4c), that is significantly wider than the spatial location uncertainty of ±50 m and is thus indicative of real features and not location artifacts. The seismicity cluster clearly outlines an almost planar feature that dips to the east (Figures 4c and Figure S3b in Supporting Information S1).

4.3. Focal Mechanisms and Hypocenter Imaging

Microearthquake focal mechanisms are useful for understanding relative shearing motions. Reliable focal mechanism solutions with maximum azimuthal gaps ≤90° and maximum takeoff angles ≤60°, were obtained for 30 events. Small magnitude events <M_L 1 were detected at stations closest to the event, limiting the maximum azimuthal gap and takeoff angles for focal mechanism solutions. The fault plane uncertainty for the 30 events ranged between 27 and 44° and all focal mechanism estimates are of quality D. Fourteen events with weighted polarity errors ≤15% and station distribution ratios ≥50% were classified as improved quality solutions. Figure S7 in Supporting Information S1 shows the uncertainty estimates for the obtained solutions.

The microearthquakes were distributed across both boundary shear zones and their focal mechanisms exhibited north-northwest to south-southeast strikes, oblique left-lateral and normal shearing with dominant dips between 50 and 85° (Figure 4c). Estimated fault planes from the hypocenter imaging (details in Text S3 in Supporting Information S1) are aligned parallel to local normal faults that intersect the top of the salt structural model of Looff (2017) (Figure 4a), and perpendicular to the regional east-west striking normal faults. The dips of 83–86° obtained from the best fit rupture planes were validated using focal mechanism solutions.

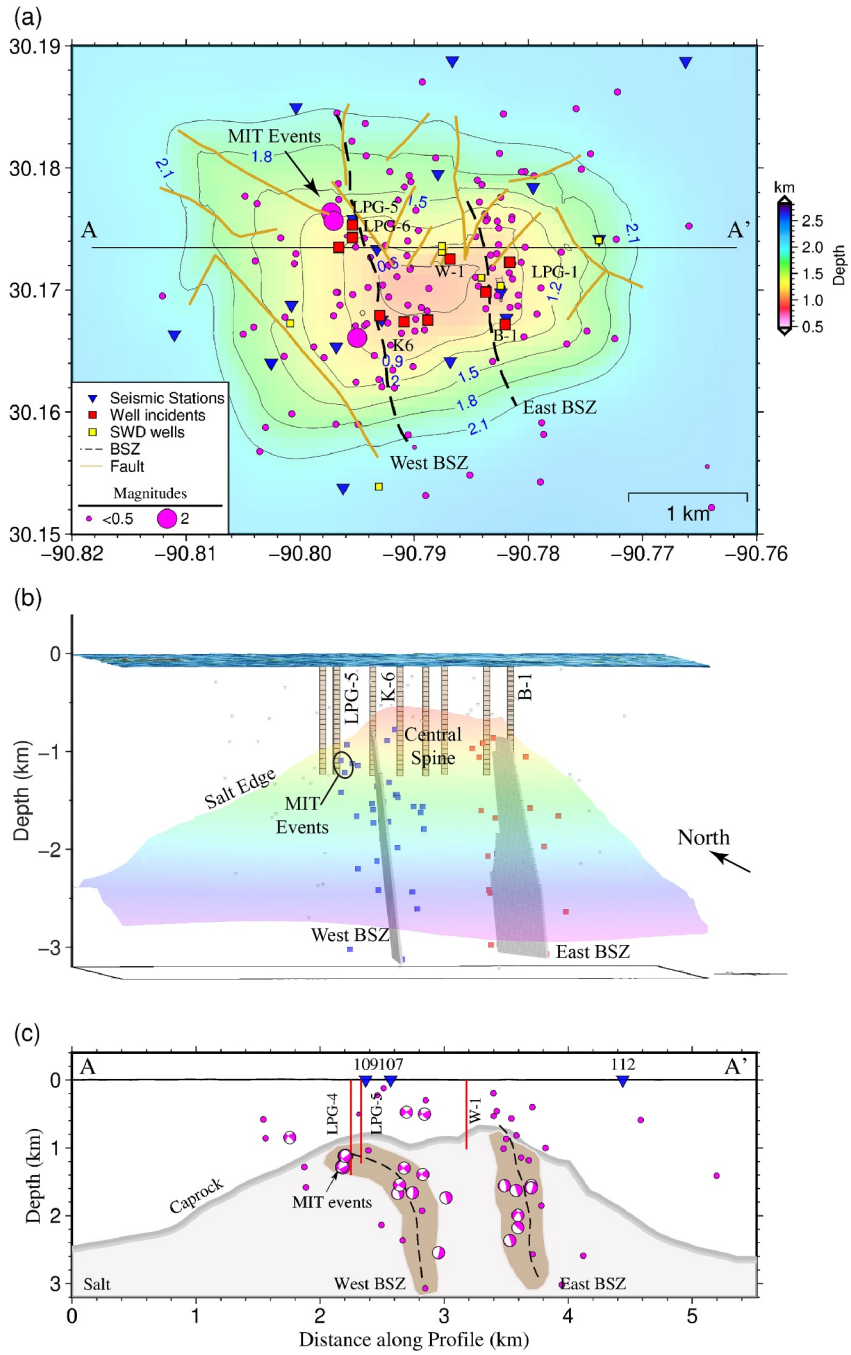

Figure 4. Microearthquake distribution across the dome. (a) Spatial distribution of microearthquakes (magenta circles) scaled by their local magnitudes. The east (Looff, 2017) and west boundary shear zones (BSZs) are shown with black dashed lines. Caprock faults are shown as light brown lines, and background shaded contours of the top of salt are modified after Looff (2017). The map view of focal mechanisms is shown in Figure S6 in Supporting Information S1. (b) View from the south showing the three-dimensional salt structure, cavern outlines (yellow), microearthquakes (blue and red dots), and the simplified extent of the two boundary shear zones as planar features. Planes of best fit through the clustered seismicity help to differentiate the boundaries between salt spines. (c) Cross-section A-A′ showing the estimated widths of the shear zones based on clustered seismicity. The microearthquakes within 300 m of the profile are shown and the focal mechanisms are viewed from the south. Projected wells are shown as red vertical lines.

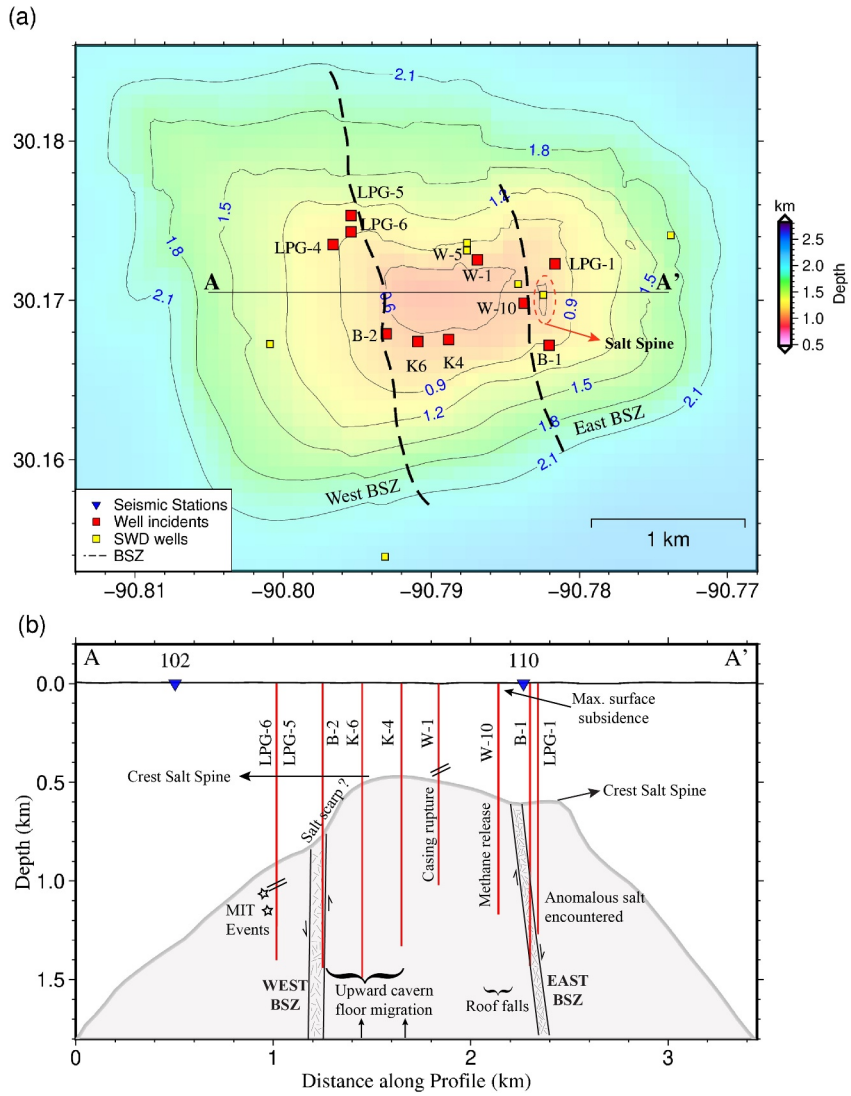

Figure 5. Independent shear zone identification with well and cavern data. (a) Map view of caverns with prior incidents relative to shear zone traces. (b) Simplified representation of BSZs as planar features with labeled cavern incidents. Projected cavern wells are shown as red vertical lines.

4.4. Changes in Cavern Shapes From Sonar Measurements

We further investigate intra-intrasalt deformation by comparing time-lapse sonar measurements to estimate the change in cavern volumes over time. Sonar surveys are an expensive way to estimate cavern volumes and cavern operators are required to acquire them every 5 years for routine monitoring or before and after workover activity (SONRIS, 2024). On the western edge of the dome, sonar measurements acquired within the LPG-5 and LPG-6 caverns from 2017 to 2021 or 2022 show small floor changes of 6 and 9 m, respectively, that translate to an average salt closure rate of 1 and 2 m/year (Figures 6a and 6b).

Within the central spine sonar measurements of the B-2, K-4, and K-6 caverns acquired in 2011 and 2021 show major changes in cavern floor height of ~90, 43, and 40 m (Figures 5b and 6c–6e). This translates to a maximum salt closure rate of nearly 8 m/year. Minimal roof migration is recorded in the K-4 and K-6 caverns, while rockfalls and secondary leaching of the B-2 cavern in 2009 caused widening of the cavern walls (Flodim, 2024). To the NE, vertical salt movement is limited near the W-1 and W-10 caverns (Figures 6f and 6g). No major changes in cavern shape were observed; however, lateral salt motion caused casing and liner ruptures along the W-1 cavern well. The magnitude of salt creep in different spines can influence variations in cavern closure rates,

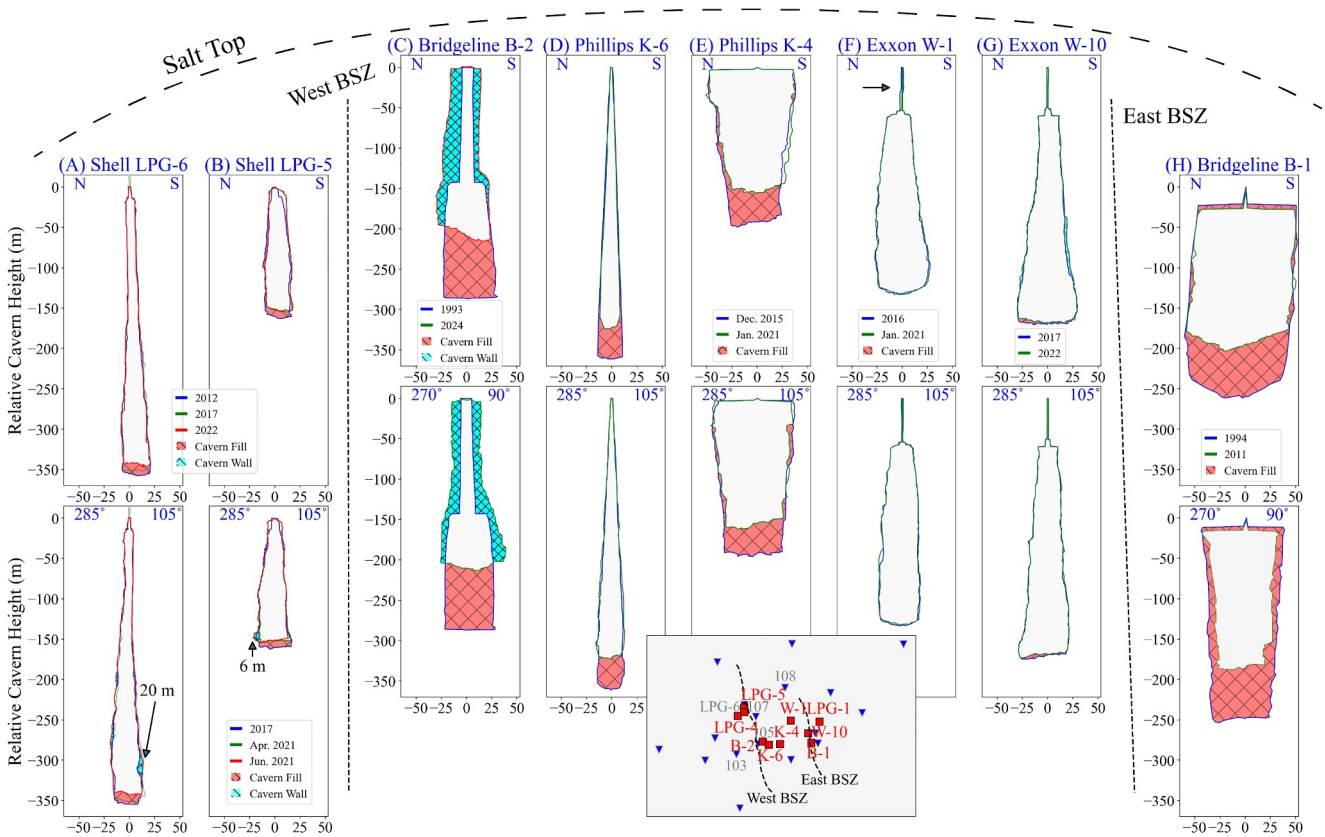

Figure 6. Timelapse cross-sections of cavern geometry obtained from sonar measurements (SONRIS, 2024). All caverns are plotted at the same scale, well names are indicated above each panel, and cavern locations are shown in the inset map. The salt top is schematically shown. Top panels show N-S cross-sections and bottom panels show approximate W-E sections, with the legends indicating the year of the sonar surveys. Changes in the cavern shape through time are indicated by cyan and red patterns.

causing some caverns to close faster than others (Bettin et al., 2017; Cyran, 2021), which is evident in the different closure rates observed at these five caverns located less than a kilometer from each other.

In the eastern part of the dome, salt creep is not as pronounced, and time-lapse sonar measurements from the B-1 cavern (Figure 6h) show evidence of roof falls and floor migration. The average salt closure rate is ~3 m/year. The B-1 cavern roof and sides are contracted along the W-E direction around the east BSZ (Figure 6h). Roof falls have also been reported within the W-10 cavern by operators (Figure 6g) (LADNR, 2022a). These variations in the cavern deformation determined from sonar measurements from west to east across the dome are indicative of differential salt movement across different spines that are separated by shear zones (Figure 5b). Transient creep along salt shear zones can lead to large deformations over short periods of time, generating the detected microearthquakes (Figures 1 and 4; Cyran, 2021).

4.5. Well Incidents

Cavern wells drilled near boundary shear zones (BSZ) and the salt edge are at risk of developing complications (Bérest et al., 2013; Ford & Dreger, 2020). Expansion of the B-2 cavern in 2009 resulted in preferential dissolution of the surrounding salt (Flodim, 2024), creating an irregular cavern geometry (Figure S8 in Supporting Information S1) that poses a cavern communication risk for the nearby K-6 cavern. Another recent incident along the west BSZ occurred in the LPG-5 cavern well. The LPG-5 well was drilled between the west BSZ and salt edge in 1973 and shut-in for several years (Figures 4c and 5b). A mechanical integrity test (MIT) was performed in 2021 to assess its stability for renewed cavern operations, and on 3 May 2021, brine was injected to raise the cavern pressure to 6.48 MPa (941.09 psi) in the production annulus followed by a 7-day stabilization period until the pressure decline reached 0.03 MPa (5.1 psi) per day (Figure 3c). The cavern lost integrity during the nitrogen injection phase of the MIT on 10 May 2021, and the casing pressure changed by more than 5%, which constitutes a

well failure incident. Casing pressures dropped from 14.86 MPa (2156 psi) to 4.62 MPa (670 psi) in less than two minutes and site workers recall feeling ground movement, hearing an audible pop, and observing the release of 220,000 scf of nitrogen at the surface (LADNR, 2021a). Following the drop in cavern pressures, two MS-I type events occurred at 22:16:34.72 UTC and 22:17:11.96 UTC, respectively, within proximity of the LPG-5 cavern (MIT events 18 and 19 in A-A′ in Figures 4c and 5b), and post-accident reports indicate casing cracks at 1,131–1,136 m depth around the microearthquake hypocentral depths of 1,259 and 1,149 m, respectively (Solutions, 2021). The microearthquakes were located west of the inferred west BSZ core (Figure 5b), within a potential damage zone where salt shearing can trigger seismicity. Additional damage was identified at the base of the cavern with sonar surveys (Figure 6b), and a 6–9 m wide by 1.5 m deep crater was observed around the well head (LADNR, 2021b).

Other incidents near the west BSZ include an emergency workover to replace the brine string in LPG-4 following its failure in Q2 2020 (LADNR, 2020b), and preferential leaching of the Bridgeline B-2 cavern (Flodim, 2024; Figure S8 in Supporting Information S1). Near the east BSZ, our review of historical well reports indicates that liner ruptures were documented 3 times approximately 1960 and 1966 in the W-5 saltwater disposal well (Consultants, 1990). Methane blowouts have also been recorded at the W-9 cavern and anomalous salt deposits were encountered within the LPG-1 and LPG-2 caverns (Figure 5b) (Looff, 2017).

4.6. Subsidence Surveys

To investigate the effect of salt migration on surface infrastructure, we reviewed subsidence measurements acquired by the salt dome operators between 2015 and 2019. Five precision level surveys were conducted using a combination of 57 monuments and wellheads (USA, 2019). We estimated relative subsidence by measuring the elevation differences between a reference benchmark (SD-01 monument) and the level-survey monuments. Changes in annual elevation were derived from elevation differences and a subsidence map was generated by linearly interpolating points between monuments (Figure S9 in Supporting Information S1). A maximum subsidence of ∼0.81 inches/year was observed west of the eastern BSZ around the Kaiser 1 well, which is plugged and abandoned (LADNR, 1986), and 320 m southwest of the Bridgeline B-1 cavern. Other notable caverns with high rates of elevation change include LPG-5, W-4, W-6, and W-7 (Figure S9 in Supporting Information S1). All these caverns occur within proximity of the shear zones, and the brittle behavior of anomalous salt can accelerate roof falls, which influences surface subsidence if cavern pressures are not properly managed. At the time of writing, no surface facilities face critical endangerment, but periodic monitoring of these caverns is recommended even after they have been plugged and abandoned.

5. Discussion

In this section, we combine observations from our microearthquake catalog with associated well data. We analyze the variations in seismicity across the salt dome and evaluate potential source mechanisms. We proceed to integrate the spatial and temporal seismicity patterns with the geological context around the salt dome, which helps us unlock new insights and evaluate the contributions of our dataset and methods.

5.1. Microearthquake Source Mechanisms in Salt Domes

Previous studies have investigated the factors that can trigger microearthquakes in salt domes. For example, at the Cerville-Buissoncourt salt mine in France, more than 200 events per hour were reported following the M_w 7.2 Kepulauan Talaud earthquake in Indonesia, and it was concluded that the events were triggered by passing surface waves (Jousset & Rohmer, 2012). We investigate the possibility of triggering from passing surface waves from remote-large earthquakes by analyzing 1820 teleseismic earthquakes with magnitudes $M_w > 5$ that occurred during the monitoring period. On the day of the well failure (10 May 2021), three teleseismic events (M_w 5–5.4, located 82–115° away) occurred within 5 min of the well failure; however, our seismic array did not detect the ground motions. Analysis of regional earthquake catalogs shows that large events occur almost daily, in contrast to our local catalog of microearthquakes that exhibit cascade-like peaks in seismicity separated by several days of no activity (Figures 3a and 3b). Subsequently, we did not find evidence of our observed microearthquakes being triggered by passing surface waves from of remote large earthquakes.

For caverns located close to the edge of the salt-sediment boundary, caprock movement from salt creep near the boundary can trigger microearthquakes (Fortier et al., 2006) and in extreme cases, sidewall cavern collapse can

trigger microearthquakes as sediments flow along the disturbed rock zone into breached caverns (Chicago Bridge, 2013; Ford & Dreger, 2020). However, our cross-section of the salt structural map with projected microearthquakes located within 300 m (Figure 4c) shows that few events occur near the salt-sediment boundary. But the majority of the microearthquakes occur deeper within the dome. Sonar surveys of caverns close to the salt edge (<125 m, LPG-5 and 6) show no indications of major sidewall damage (Figures 6a and 6b) and the subsidence values above those caverns (Figure S9 in Supporting Information S1) are within relatively safe thresholds (USA, 2019). While the predominant source mechanism for the identified events does not appear to be caprock movement or sidewall collapse, we advocate for the continuous seismic and sonar monitoring of the LPG-5 cavern considering that it sustained sidewall damage during the well failure event (Figure 6b), and its proximity to the salt-sediment boundary (Figure 5b).

We investigated the plausibility of the microearthquakes being generated by roof falls within the caverns. Roof falls modify the geometry of caverns and can be monitored using sonar surveys. Falling blocks of salt or overlying sediment in caverns generate high frequency microearthquakes upon impact with the bottom of the cavern that can be recorded by nearby seismometers. The soluble portions of the blocks are dissolved in cavern brines, while the insoluble blocks fill the base of the cavern. This effect has been observed at the Geosel-Manosque, Cerville-Buissoncourt, and Verkhnekamskoye salt deposits in Europe, and sinkholes around the Dead Sea region (Fortier et al., 2006; Malovichko, 2009; Mercerat et al., 2009; Wust-Bloch & Joswig, 2006). For example, well logs at the Cerville-Buissoncourt dome recorded a roof migration of 6 m in 1 year, and a final roof height difference of 25 m over the operating period of the cavern. At Sorrento, timelapse sonar surveys of the B-1 cavern revealed a 4 m roof migration, and roof falls were reported in the W-10 cavern (Figures 5b and 6g–6h) (LADNR, 2022a). These observations suggest possible block drop seismicity. However, the location of our microearthquakes at depths below and outside the caverns (Figure 4b), along with sonar surveys in other caverns displaying relative roof stability while exhibiting cavern floor migration (Figures 6a–6e) implies the existence of other source mechanisms within the Sorrento dome.

Although rocks falling from the roof cannot explain upward cavern floor migration with a stable roof, upward salt migration, which contributes to increased cavern closure rates, can explain these observations (Bérest et al., 2013). The clustered microearthquakes align with mapped shear zones from drilled wells (Figures 4c and 5b), where salt creep reactivates preexisting fractures in anomalous salt bodies (Davison, 2009) (Figure 1d). Salt creep along a shear zone is capable of overstretching well casing, causing the casing and liner ruptures observed in the LPG-4, LPG-5, W-1 and W-5 wells (Figures 5 and 6; Lord, 2013). Salt creep and shear zone deformation within salt domes have been linked to gas outbursts, increased shearing, slickenside occurrence, and halite recrystallization at other Gulf Coast domes (Bérest et al., 2019; Davison, 2009; Neal et al., 1993). At Sorrento, drilled wells within the vicinity of the shear zones were reported to have methane outbursts, preferentially leached cavern geometries, anomalous salt properties, and ruptured well casings (Looff, 2017). This suggests that internal shearing of salt is the dominant source of microearthquake activity at the Sorrento dome.

5.2. Effect of Salt Creep on Shear Zones

While the concept of salt creep is well understood and even accounted for in geomechanical models (Sandia, 2017), shear zone identification and its potential hazards are poorly understood and often overlooked. During normal storage operations, wellhead pressure steadily increases in caverns due to salt creep, and this pressure is usually bled off when it exceeds the operating pressure range as part of a pressure cycle (Bettin et al., 2017). During workovers, the caverns are completely depressurized, which can result in accelerated salt creep along the shear zones (Bérest et al., 2013). Salt creep along the shear zones can trigger microearthquakes, increasing the risk of casing breach and gas release during well workovers like a mechanical integrity test. Based on the proximity of the LPG-5 cavern to the west BSZ (Figures 4c and 5b) and the low cavern pressures during the workover process, we conclude that accelerated shear movement weakened the well casing to the point of failure, following which impulsive energy from the MIT events exacerbated the damage (Figure 3c), resulting in the gas release observed at the surface, and associated wellhead damage.

5.3. Geological Context of Salt Dome Seismic Hazards

When assessing seismic hazards, we need to evaluate all the avalaible subsurface data. Well logs, sonar measurements and hanging string failure events are useful for monitoring cavern integrity at specific points in time.

However, due to data sparsity (acquisition timeframe and limited sample points), it is difficult to use them to independently assess unstable regions within the salt dome unless an obvious failure occurs (B. L. Ehgartner & Sobolik, 2009). In contrast, seismicity is useful for mapping the 3D extent of shear zones, identifying weak zones that are actively undergoing seismic deformation (seismogenic regions), and improving near real-time hazard mapping in salt dome cavern facilities (Mercerat et al., 2009). Independently, both data types provide distinct advantages. However, together they can be integrated to robustly assess seismic hazards. For instance, when the microearthquakes are integrated with well data, the dip of the east BSZ microearthquakes explains how the LPG-1 and LPG-2 wells encountered anomalous salt deposits considering they were drilled east of the shear zone (Figure 5b). The gaps in seismicity between the two BSZs suggest three potential spines migrating upwards at different rates. The central salt spine is migrating the fastest, as evidenced by the high cavern closure rates within the B-2, K-4, and K-6 caverns (Figures 6c–6e), and the relatively thinner overburden thickness above the spine. To the east and west, the other salt spines are much smaller and relegated to the flanks of the central spine. Considering that salt spines discussed in the literature are circular in shape (Warren, 2016), we could have E-W trending shear zones that were not imaged in our current catalog. Additional months of seismic monitoring can be combined with downhole sensors to improve the number of intra-salt event detections, and accuracy of event locations for further shear zone imaging.

For operators, temporal seismicity trends can provide insights into salt instability during workover or drilling operations. However, interpreters have to be careful when analyzing such trends. While a departure from background seismicity trends can be indicative of impending damage, time to failure models cannot be derived from seismicity alone (Ford & Dreger, 2020; Petersen et al., 2006). The number of recorded events depends on noise levels, salt creep, and station distribution, as evidenced by the higher number of daily recorded micro-earthquakes during the facility shut-down in comparison to the LPG-5 well failure event (Figure 3a). In this study, our integration of seismic and well data allows us to associate event spikes with well incidents and improve our understanding of hazard at the Sorrento salt dome.

Considering the distance to the salt edge and microseismicity distribution, we propose that the safest region for cavern operations is above the central spine, between the two identified BSZs at depths <1.3 km (Figure 4b). Caverns located on the flanks away from the central spine are closer to the salt edge, which increases the risk of additional complications during operations. One draw-back for leaching the central spine is the high surface subsidence near the shear zones, and fast closure rate observed in the K-4 and K-6 caverns (Figures 5b, 6c, and 6d). Additional cavern wells will need to avoid those regions to minimize associated subsurface hazards. By avoiding the salt around the shear zones, the risk of casing breach due to seismicity is relatively lower.

As more salt domes are enlisted for energy storage as part of the energy transition, the environmental safety of cavern operations becomes increasingly crucial. Integrating microseismic monitoring into site evaluation criteria for new sites and deploying a combination of borehole and surface nodal arrays for passive monitoring of existing underground storage facilities are key strategies. These approaches enable operators to proactively identify ground movement on seismic instruments and take steps to minimize the risk of blowouts or sinkhole formation.

6. Conclusion

Similar to other machine learning earthquake detection models (Mousavi et al., 2020; Ross et al., 2018; Zhu & Beroza, 2019), we detect microearthquakes using 3-component waveforms however, our model is more efficient at detecting salt dome microearthquakes because it was trained and finetuned with small microearthquakes ($M_w < 3$) from both tectonic and salt dome environments. We successfully apply our Hybrid U-Net machine learning model for microearthquake detection at the Sorrento salt dome, and combined our event catalog with existing well data and published literature to generate a holistic assessment of seismic hazard. The detected events with magnitudes ranging between M_L −3 and 2 were correlated with salt creep and fracture reactivation along two internal boundary shear zones where seismicity triggers cavern deformation. Our geological interpretation accurately explains past and recent incidents, and we propose recommendations to improve the safety of cavern operations.

Our pre-trained machine learning model is easy to use and can be finetuned to monitor other sites with limited seismicity catalogs such as nuclear plants, dams, and bridges. It is also useful for detecting seismicity from other hazards such as landslides and mine collapses, and identifying BSZs at other sites used for underground storage. BSZ identification is of central importance if salt domes are to be utilized for hydrogen storage during the energy

transition because hydrogen has lower molecular weight than natural gas and can escape into even smaller cracks. In this study, we have demonstrated that salt dome characterization can be optimized with microearthquake monitoring to identify seismogenic BSZs prior to leaching salt caverns, allowing preferential location of caverns within stable salt, which extends their lifecycles when used for natural gas and hydrogen storage.

Data Availability Statement

All data needed to evaluate the conclusions in the paper are presented in the paper and/or Supporting Information S1. The waveform data from the Sorrento array are publicly available at the SAGE Facility Web Services (https://service.iris.edu/irisws/) under the ZE network (Persaud, 2020). The trained model used for event detection, catalogs of the detected events, and scripts to reproduce the images are available at the Zenodo repository (Omojola & Persaud, 2024). Data analysis was carried out using different python packages. ObsPy was used for processing the seismic data (Krischer et al., 2017). All plots were created with Matplotlib and PyGMT 6.0.0 (Hunter & Dale, 2007; Uieda et al., 2021). The hybrid autoencoder model was built with TensorFlow 2.5, and shapefiles were processed using Geopandas (Abadi et al., 2015; Jordahl et al., 2020).

Acknowledgments

We thank the operators at the Sorrento salt dome in Ascension Parish, Louisiana, for providing access to the sites occupied by our seismic array. We are grateful to Justin Kain and Jeff Nunn for their help installing the instruments and to Jeff Hanor for discussions on the salt domes. We thank the USGS Lower Mississippi-Gulf Water Science Center for releasing the preliminary data from the Bayou Conway station. Most computations were carried out on the LSU HPC SuperMike II cluster. Some of the seismic instruments were provided by the United States Geological Survey and Earthscope through the Earthscope Primary Instrument Center (EPIC, formerly the PASSCAL Instrument Center) at New Mexico Tech. This material is based upon work supported by the National Science Foundation under Grant (2045983). The facilities of the Earthscope Consortium are supported by the National Science Foundation's Seismological Facilities for the Advancement of Geoscience (SAGE) Award under Cooperative Support Agreement EAR-1851048. Constructive comments from our reviewers helped improve the quality of this material.

References

Abadi, M., Agarwal, A., Barham, P., Brevdo, E., Chen, Z., Citro, C., et al. (2015). TensorFlow: Large-scale machine learning on heterogeneous systems.

Bauer, S. J., Ehgartner, B. L., & Neal, J. T. (1997). *Geotechnical studies associated with decommissioning the strategic petroleum reserve facility at Weeks Island, Louisiana: A case history*. Sandia National Lab. (SNL-NM). Retrieved from https://digital.library.unt.edu/ark:/67531/metadc677438/

Beckman, K., Determeyer, P., & Mowrey, E. (1995). Natural gas storage: Historical development and expected evolution. Final report Final report, December 1994–February 1995. Retrieved from https://ntrl.ntis.gov/NTRL/dashboard/searchResults/titleDetail/PB95249900.xhtml#

Bérest, P., Djakeun-Djizanne, H., Brouard, B., & Hévin, G. (2013). Rapid Depresurizations: Can they lead to irreversible damage? In *Solution Mining Research Institute Spring 2012 Technical Conference*. https://doi.org/10.48550/arXiv.1302.2582

Bérest, P., Réveillère, A., Evans, D., & Stöwer, M. (2019). Review and analysis of historical leakages from storage salt caverns wells. In *Oil & Gas Science and Technology–Revue d'IFP Energies nouvelles* (Vol. 74, p. 27). https://doi.org/10.2516/ogst/2018093

Bettin, G., Hart, D., Sobolik, S. R., Park, B., & Lord, A. C. S. (2017). Depressurization effects in salt dome caverns.

Caglayan, D. G., Weber, N., Heinrichs, H. U., Linßen, J., Robinius, M., Kukla, P. A., & Stolten, D. (2020). Technical potential of salt caverns for hydrogen storage in Europe. *International Journal of Hydrogen Energy*, *45*(11), 6793–6805. https://doi.org/10.1016/j.ijhydene.2019.12.161

Chicago Bridge, I. C. C. I. (2013). *Blue Ribbon Commission Initial Technical Briefing*. Louisiana State University. Retrieved from http://www.dnr.louisiana.gov/assets/OC/BC_All_Updates/Plans_Reports/BlueRibb.04.05.13.pdf

Consultants, W.-C. (1990). Injection Well Investigation Workplan [Report](970152). (submitted to Exxon Pipeline Company Sorrento Facility, Louisiana) Retrieved from https://sonlite.dnr.state.la.us/dnrservices/redirectUrl.jsp?dDocname=14268206&showInline=True

Cyran, K. (2021). The influence of impurities and fabrics on mechanical properties of rock salt for underground storage in salt caverns–a review. *Archives of Mining Sciences*, *66*(2), 155–179.

Davison, I. (2009). Faulting and fluid flow through salt. *Journal of the Geological Society*, *166*(2), 205–216. https://doi.org/10.1144/0016-76492008-064

Di Grazia, G., Langer, H., Ursino, A., Scarfì, L., & Gresta, S. (2001). On the estimate of earthquake magnitude at a local seismic network. *Annals of Geophysics*, *44*(3). https://doi.org/10.4401/ag-3577

Dreger, D. S., & Ford, S. R. (2020). Pre-Sinkhole Seismicity at the Napoleonville Salt Dome: Implications for Local Seismic Monitoring of Underground Caverns. *Seismological Research Letters*, *91*(3), 1672–1678. https://doi.org/10.1785/0220190224

Ehgartner, B., Neal, J., & Hinkebein, T. (1998). *Gas releases from salt*. A. Sandia National Lab. (SNL-NM), NM (United States). https://doi.org/10.2172/656531

Ehgartner, B. L., & Sobolik, S. R. (2009). Analysis of cavern stability at the West Hackberry SPR site. Retrieved from https://www.osti.gov/servlets/purl/959096

EIA. (2012). Natural Gas Interstate and Intrastate Pipelines EIA from FERC and other external sources eia.gov/maps/map_data/NaturalGas_InterIntrastate_Pipelines_US_EIA.zip.

Evans, D. J. (2007). An appraisal of Underground Gas Storage technologies and incidents, for the development of risk assessment methodology. Volume 1, Text. Volume 2, Figures and Tables.

Evans, D. J., & Schultz, R. A. (2017). Analysis of occurrences at underground fuel storage facilities and assessment of the main mechanisms leading to loss of storage integrity. In *ARMA US Rock Mechanics/Geomechanics Symposium*.

Flodim, S. (2024). Sonar Report with Overlays by Flodim Sonar Surveys—May 6, 2024 Bridgeline B2 [FORM UIC-7](972030). (submitted to the Louisiana Department of Natural Resources, Office of Conservation, Injection and Mining Division) Retrieved from https://sonlite.dnr.state.la.us/dnrservices/redirectUrl.jsp?dID=14901677&showInline=True&nativeFile=True

Ford, S. R., & Dreger, D. S. (2020). Pre-Sinkhole Seismicity at the Napoleonville Salt Dome: Implications for Local Seismic Monitoring of Underground Caverns. *Seismological Research Letters*, *91*(3), 1672–1678. https://doi.org/10.1785/0220190224

Fortier, E., Renoux, P., & Maisons, C. (2006). Seismic monitoring of underground storage in salt cavity in a seismo-tectonic context. In *First EAGE Passive Seismic Workshop-Exploration and Monitoring Applications*. https://doi.org/10.3997/2214-4609.201402590

Gillhaus, A., & Horvath, P. (2008). *Compilation of geological and geotechnical data of worldwide domal salt deposits and domal salt cavern fields*. Solution Mining Research Insitute and KBB Underground Technologies GmbH.

Glorot, X., Bordes, A., & Bengio, Y. (2011). Deep sparse rectifier neural networks. In *Proceedings of the Fourteenth International Conference on Artificial Intelligence and Statistics*.

Hanusik, V. R., & Katy (2019). When the Ground Gives Way. Retrieved from https://placesjournal.org/article/when-the-ground-gives-way-bayou-corne-sinkhole/?cn-reloaded=1

Hardebeck, J. L., & Shearer, P. M. (2008). HASH: A FORTRAN Program for Computing Earthquake First-Motion Focal Mechanisms–v1.2. Retrieved from https://www.geo.uib.no/seismo/SOFTWARE/SEISAN/OLDER_VERSIONS/SEISAN_10.4.1/alpha/LIN64/INF/hash.pdf

Hunter, J., & Dale, D. (2007). The matplotlib user's guide. In *Matplotlib 0.90. 0 user's guide*.

Ioffe, S. (2015). Batch normalization: Accelerating deep network training by reducing internal covariate shift. *arXiv*, *3*. https://doi.org/10.48550/arXiv.1502.03167

Jackson, C. A.-L., Jackson, M. P., Hudec, M. R., & Rodriguez, C. R. (2015). Enigmatic structures within salt walls of the Santos Basin—Part 1: Geometry and kinematics from 3D seismic reflection and well data. *Journal of Structural Geology*, *75*, 135–162. https://doi.org/10.1016/j.jsg.2015.01.010

Jacoby, C. (1977). Geology—Hydrology of Avery Island Salt Dome by Jacoby and Co., Dalton, Pa. (USA) (the Department of Energy). Retrieved from https://www.osti.gov/servlets/purl/5142591

Jordahl, K., den Bossche, J., Fleischmann, M., Wasserman, J., McBride, J., Gerard, J., et al. (2020). Geopandas/Geopandas: V0. 8.1. 2020. https://doi.org/10.5281/zenodo.3946761

Jousset, P., & Rohmer, J. (2012). Evidence for remotely triggered microearthquakes during salt cavern collapse. *Geophysical Journal International*, *191*(1), 207–223. https://doi.org/10.1111/j.1365-246X.2012.05598.x

Juez-Larré, J., Van Gessel, S., Dalman, R., Remmelts, G., & Groenenberg, R. (2019). Assessment of underground energy storage potential to support the energy transition in The Netherlands. *First Break*, *37*(7), 57–66. https://doi.org/10.3997/1365-2397.n0039

Kinscher, J., Bernard, P., Contrucci, I., Mangeney, A., Piguet, J.-P., & Bigarre, P. (2015). Location of microseismic swarms induced by salt solution mining. *Geophysical Journal International*, *200*(1), 337–362. https://doi.org/10.1093/gji/ggu396

Klein, F. W. (2002). *User's guide to HYPOINVERSE-2000, a Fortran program to solve for earthquake locations and magnitudes (2331–1258)*. US Geological Survey.

Krischer, L., Megies, T., Sales de Andrade, E., Barsch, R., & MacCarthy, J. (2017). ObsPy: A Python Toolbox for Seismology. In *EGU General Assembly Conference Abstracts*.

Kupfer, D. H. (1990). Anomalous features in the Five Islands salt stocks, Louisiana. In *Gulf Coast Association of Geological Societies Transactions, XL* (pp. 425–537). Retrieved from https://archives.datapages.com/data/gcags/data/040/040001/0425.htm

LADNR. (1986). Plug and Abandon report for Kaiser-1 Well [FORM UIC-002344](073457). (submitted to the Louisiana Department of Natural Resources, Office of Conservation, Injection and Mining Division) Retrieved from https://sonlite.dnr.state.la.us/dnrservices/redirectUrl.jsp?dDocname=14106287&showInline=True&nativeFile=True

LADNR. (2020a). Findings of Facts at the Sorrento Salt dome (IMD 2020-03). (submitted to the Department of Natural Resources, Office of Conservation, Baton Rouge, Louisiana) Retrieved from https://sonlite.dnr.state.la.us/dnrservices/redirectUrl.jsp?dDocname=13446796&showInline=True&nativeFile=True

LADNR. (2020b). Quarterly Cavern Summary Report at LPG-04 for Q2 2020 [FORM UIC-7](971517). (submitted to the Louisiana Department of Natural Resources, Office of Conservation, Injection and Mining Division) Retrieved from https://sonlite.dnr.state.la.us/dnrservices/redirectUrl.jsp?dDocname=13519001&showInline=True&nativeFile=True

LADNR. (2021a). Class II Well Test / Inspection Report at LPG-05 on 12 May 2021 [FORM UIC-7](971518). (submitted to the Louisiana Department of Natural Resources, Office of Conservation, Injection and Mining Division) Retrieved from https://sonlite.dnr.state.la.us/dnrservices/redirectUrl.jsp?dDocname=13729513&showInline=True&nativeFile=True

LADNR. (2021b). Class II Well Test / Inspection Report at LPG-05 on 19 May 2021 [FORM UIC-7](971518). (submitted to the Louisiana Department of Natural Resources, Office of Conservation, Injection and Mining Division) Retrieved from https://sonlite.dnr.state.la.us/dnrservices/redirectUrl.jsp?dDocname=13729514&showInline=True&nativeFile=True

LADNR. (2022a). LPG W-10 Log Interpretation Summary and Certification Report [Report](971569). (submitted to the Louisiana Department of Natural Resources, Office of Conservation, Injection and Mining Division) Retrieved from https://sonlite.dnr.state.la.us/dnrservices/redirectUrl.jsp?dDocname=14475696&showInline=True&nativeFile=True

LADNR. (2022b). LPG W-4 Salt Cavern Weekly Monitoring Log and Summary Report for Q2 2022 [FORM UIC-50](971896). (submitted to the Louisiana Department of Natural Resources, Office of Conservation, Injection and Mining Division) Retrieved from https://sonlite.dnr.state.la.us/dnrservices/redirectUrl.jsp?dDocname=14088242&showInline=True&nativeFile=True

Looff, K. (2017). The Impact of Anomalous Salt and Boundary Shear Zones on Salt Cavern Geometry, Cavern Operations, and Cavern Integrity. In *Proceedings of SMRI Spring Meeting, Albuquerque, New Mexico*.

Lord, A. S. (2013). *Holistic Understanding of the Big Hill Salt Dome Geologic Processes in Relation to Impacts on Cavern Well Integrity*. Solution Mining Research Institute. Retrieved from https://www.osti.gov/servlets/purl/1116002

Lord, A. S. (2009). Overview of geologic storage of natural gas with an emphasis on assessing the feasibility of storing hydrogen. Retrieved from https://www.osti.gov/biblio/975258

Malovichko, D. (2009). Study of the seismic source mechanisms in mines of the Verkhnekamskoye potash deposit. In C. Tang (Ed.), *Proceedings of 7th International Symposium onRockbursts and Seismicity in Mines: Controlling Seismic Hazard and Sustainable Development of Deep Mines*.

Mercerat, E. D., Driad-Lebeau, L., & Bernard, P. (2009). Induced Seismicity Monitoring of an Underground Salt Cavern Prone to Collapse. *Pure and Applied Geophysics*, *167*(1–2), 5–25. https://doi.org/10.1007/s00024-009-0008-1

Mitchell, D. (2018). *Judge: Fault for Bayou Corne sinkhole lies with Texas Brine, OxyChem, Vulcan; companies had decades of warnings*. The Advocate. Retrieved from https://www.theadvocate.com/baton_rouge/news/article_7856ff5e-f4ae-11e7-b86c-4f261682612b.html

Mousavi, S. M., Ellsworth, W. L., Zhu, W., Chuang, L. Y., & Beroza, G. C. (2020). Earthquake transformer—An attentive deep-learning model for simultaneous earthquake detection and phase picking. *Nature Communications*, *11*(1), 1–12. https://doi.org/10.1038/s41467-020-17591-w

Mousavi, S. M., Sheng, Y., Zhu, W., & Beroza, G. C. (2019). STanford EArthquake Dataset (STEAD): A global data set of seismic signals for AI. *IEEE Access*, *7*, 179464–179476. https://doi.org/10.1109/ACCESS.2019.2947848

Nayak, A., & Dreger, D. S. (2018). Source inversion of seismic events associated with the sinkhole at Napoleonville salt dome, Louisiana using a 3-D velocity model. *Geophysical Journal International*, *214*(3), 1808–1829. https://doi.org/10.1093/gji/ggy202

Nayak, A., & Douglas, S. (2014). Moment Tensor Inversion of Seismic Events Associated with the Sinkhole at Napoleonville Salt Dome, Louisiana. *Bulletin of the Seismological Society of America*, *104*(4), 1763–1776. https://doi.org/10.1785/0120130260

Neal, J. T., Magorian, T., Thoms, R., Autin, W., McCulloh, R., Denzler, S., & Byrne, K. (1993). Anomalous zones in Gulf Coast salt domes with special reference to Big Hill, TX, and Weeks Island, LA.

Neal, J. T., & Myers, R. E. (1994). Salt dissolution sinkhole at the Weeks Island, Louisiana, strategic petroleum reserve storage site by Sandia National Labs. (submitted to the Department of Energy, US.) Retrieved from https://www.osti.gov/servlets/purl/10106436

Oktay, O., Schlemper, J., Folgoc, L. L., Lee, M., Heinrich, M., Misawa, K., et al. (2018). Attention u-net: Learning where to look for the pancreas. *arXiv preprint arXiv:1804.03999*.

Omojola, J., & Persaud, P. (2024). Monitoring Salt Domes Used for Energy Storage with Microseismicity: Insights for a Carbon-Neutral Future [Dataset]. *Zenodo*. https://doi.org/10.5281/zenodo.10799264

Persaud, P. (2020). Monitoring seismicity in Louisiana [Dataset]. *International Federation of Digital Seismograph Networks (International Federation of Digital Seismograph Networks)*. 2045983. https://doi.org/10.7914/SN/ZE_2020

Petersen, T., Caplan-Auerbach, J., & McNutt, S. R. (2006). Sustained long-period seismicity at Shishaldin Volcano, Alaska. *Journal of Volcanology and Geothermal Research*, *151*(4), 365–381. https://doi.org/10.1016/j.jvolgeores.2005.09.003

Petroleum, L. (2009). *Leed Successfully Flow Tests Sorrento Salt Dome in Louisiana*. Rigzone. Retrieved from https://www.rigzone.com/news/oil_gas/a/80374/leed_successfully_flow_tests_sorrento_salt_dome_in_louisiana/

Plimpton, H., Foster, R., Risbeck, J., Rutherford, R., King, F., Buffington, G., & Traweek, W. (1980). Final Report of Mine Explosion Disaster, Belle Isle Mine, Cargill, Inc. https://books.google.com/books/about/Final_report_of_mine_explosion_disaster.html?id=eOJ8_-p1eFoC

Rautman, C. A., Looff, K. M., & Looff, K. M. (2010). A Three-Dimensional Geometric Model of the Bayou Choctaw Salt Dome Southern Louisiana Using 3-D Seismic Data by Sandia National Lab.(SNL-NM), Albuquerque, NM (United States). (submitted to the US Department of Energy National Nuclear Security Administration (NNSA)) Retrieved from https://www.osti.gov/servlets/purl/1124260

Ronneberger, O., Fischer, P., & Brox, T. (2015). U-net: Convolutional networks for biomedical image segmentation. In *International Conference on Medical Image Computing and Computer-Assisted Intervention*. https://doi.org/10.1007/978-3-319-24574-4_28.pdf

Ross, Z. E., Meier, M. A., Hauksson, E., & Heaton, T. H. (2018). Generalized Seismic Phase Detection with Deep LearningShort Note. *Bulletin of the Seismological Society of America*, *108*(5A), 2894–2901. https://doi.org/10.1785/0120180080

Sainburg, T., Thielk, M., & Gentner, T. Q. (2020). Finding, visualizing, and quantifying latent structure across diverse animal vocal repertoires. *PLoS Computational Biology*, *16*(10), e1008228. https://doi.org/10.1371/journal.pcbi.1008228

Sandia, G. (2017). Sorrento Dome, Ascension Parish Louisiana—Geomechanical Assessment Of Shell LPG #3, #4, #5 And #6 (SOE160297-RPT-0003). (submitted to the Louisiana Department of Natural Resources, Office of Conservation, Injection and Mining Division).

Schlumberger. (2004). ExxonMobil Sorrento Salt Dome SWD 13 Sonic Well Log [Well Log](971518). Retrieved from https://sonlite.dnr.state.la.us/dnrservices/redirectUrl.jsp?dDocname=13734607&showInline=True&nativeFile=True

Seni, S., Mullican, W., III., & Hamlin, H. (1984). Texas salt domes—Natural resources, storage caverns, and extraction technology: The University of Texas at Austin, Bureau of Economic Geology, report prepared for Texas Department of Water Resources under interagency contract no (Texas Department of Water Resources). Retrieved from https://www.beg.utexas.edu/files/publications/contract-reports/CR1985-Seni-1.pdf

Solutions, C. (2021). Updated Wellbore Schematic Diagram (WSD)—July 2021 LPG STORAGE 005 (SN 971518). (submitted to the Louisiana Department of Natural Resources, Office of Conservation, Injection and Mining Division) Retrieved from https://sonlite.dnr.state.la.us/dnrservices/redirectUrl.jsp?dDocname=13855784&showInline=True&nativeFile=True

SONRIS, L. (2024). Louisiana Department of Natural Resources—Strategic Online Natural Resources Information system (SONRIS). Retrieved from https://www.sonris.com/

SPR, U. D. (2022). United States Department of Energy—Strategic Petroleum Reserves. Retrieved from https://www.energy.gov/fe/services/petroleum-reserves/strategic-petroleum-reserve/spr-storage-sites

Truttmann, S., Diehl, T., & Herwegh, M. (2023). Hypocenter-based 3D Imaging of Active Faults: Method and Applications in the Southwestern Swiss Alps. *Journal of Geophysical Research: Solid Earth*, *128*(6), e2023JB026352. https://doi.org/10.1029/2023JB026352

Uieda, L., Tian, D., Leong, W., Toney, L., Schlitzer, W., Grund, M., et al. (2021). PyGMT: A Python interface for the generic mapping tools. https://doi.org/10.5281/zenodo.5607255

USA, W. (2019). Precision Level Surveys and Subsidence Analysis, Sorrento Salt Dome, 2019 Report (WSP-0513). (submitted to the Louisiana Department of Natural Resources, Office of Conservation, Injection and Mining Division) Retrieved from https://sonlite.dnr.state.la.us/dnrservices/redirectUrl.jsp?dDocname=13406559&showInline=True&nativeFile=True

Waldhauser, F. (2001). hypoDD—A program to compute double-difference hypocenter locations. https://doi.org/10.7916/D8P276P1/download

Warren, J. K. (2016). *Evaporites: A geological compendium* (2 ed.). Springer. https://doi.org/10.1007/978-3-319-13512-0

Warren, J. K. (2017). Salt usually seals, but sometimes leaks: Implications for mine and cavern stabilities in the short and long term. *Earth-Science Reviews*, *165*, 302–341. https://doi.org/10.1016/j.earscirev.2016.11.008

Wijermars, E. (2013). Geomechanical modelling and subsidence prediction of salt deposits for solution mining.

Wust-Bloch, G. H., & Joswig, M. (2006). Pre-collapse identification of sinkholes in unconsolidated media at Dead Sea area by "nanoseismic monitoring" (graphical jackknife location of weak sources by few, low-SNR records). *Geophysical Journal International*, *167*(3), 1220–1232. https://doi.org/10.1111/j.1365-246X.2006.03083.x

Zhu, W., & Beroza, G. C. (2019). PhaseNet: A deep-neural-network-based seismic arrival-time picking method. *Geophysical Journal International*, *216*(1), 261–273. https://doi.org/10.1093/gji/ggy423